Research Article | Vol. 28, No. 5 / 2 March 2020 / Optics Express 7707
Optics EXPRESS

Superresolution quantitative imaging based on superoscillatory field

FAN YIN, CHANG CHEN,* WEIDONG CHEN, WEN QIAO, AND JIAN GUAN

School of IST, University of Science and Technology of China, Hefei, 230022, China
*chench@ustc.edu.cn

Abstract: The superresolution imaging of high-contrast objects is of great interest to many researchers. We propose a new method to achieve superresolution in inverse-scattering imaging of high-contrast dielectric objects. In the scheme of nonlinear inverse scattering, spatial superoscillatory incident fields are designed and applied in this research in order to retain the high-spatial-frequency components of the objects. The reconstruction results show that the proposed method resolves two objects with spacing 0.13λ. Compared with the orbital angular momentum (OAM)-carrying fields that compose a typical superoscillatory wave, the designed waveform is capable of achieving superresolution over the entire region of interest (ROI), while OAM possesses a limited superresolution area near the center of the ROI, which verifies the effectiveness of the proposed method.

1. Introduction

In the field of inverse-scattering imaging, an evanescent wave, which is the high-frequency component of the radiation field's spatial spectrum, contains the fine-scale details of the probed objects. However, evanescent waves attenuate sharply with propagation due to the low-pass spatial filtering effects of Green's function. Therefore, the spatial spectrum of the field is limited to the interval $(0, k_0]$, which results in the Rayleigh resolution limit [1,2]. To surpass the Rayleigh limit, superresolution in inverse-scattering imaging has become an active area in the relevant research fields. According to different types of approaches, superresolution methods can be categorized as physical methods or mathematical methods.

As the high-spatial-frequency information of probed objects is carried by evanescent waves, most physical superresolution methods are developed to make use of evanescent waves. Physical superresolution methods can be classified into three categories: evanescent wave amplification [3,4], coupling evanescent modes into propagating modes [5–8], and utilization of superoscillation effects [9–19]. The first two approaches rely on the materials arranged near the objects, which limits their application to the case of cooperative objects.

The last method is the utilization of superoscillation ripples that vary faster than the highest Fourier component, which makes it possible to achieve superresolution without evanescent waves [9]. Superoscillation has been applied to optical superresolution imaging by a designed mask that creates subwavelength spots of multifrequency waves without contributions from evanescent fields [9–13]. In microwave imaging, a temporal superoscillatory pulse has been designed and applied in point spread functions (PSF) to increase the range resolution of radar systems [14–16]. However, the existing superoscillation synthesis methods are based on bandlimited functions with multiple frequencies [18–23]. As electromagnetic fields are functions varying in the space domain, the synthesis of a superoscillatory field requires basis functions with different spatial spectra, and the synthesized field is a time-varying field, which is unsuitable for inverse scattering imaging analysis in time-harmonic fields. Thus, a superoscillation synthesis method for electromagnetic waves with single frequencies is studied in this paper. There is a typical single-frequency superoscillatory field, the OAM-carrying wave [17]. The OAM-based superresolution

#384866 https://doi.org/10.1364/OE.384866
Journal © 2020 Received 3 Dec 2019; revised 17 Feb 2020; accepted 19 Feb 2020; published 28 Feb 2020

Optics EXPRESS

method also takes advantage of the superoscillation property of its vortex waveform. Thus, the OAM-carrying wave is compared with our proposed superoscillatory field synthesized with a single frequency. To make full use of the high-frequency information in the electromagnetic field, the scattering model and the mathematical method have to be chosen carefully. In the linear imaging method, weak scattering assumption is applied with low-contrast objects, and the Green function in free space is a linear operator that performs as a spatial low-pass filter with a passband under free space wavenumbers [24,25]. Thus, the resolution of objects reconstructed using the linear model is limited by the Green function [26]. The contrast source inversion (CSI) method is a typical and effective nonlinear optimization method. The CSI method avoids the nonlinear relationship between the field and objects by solving a source-type integral equation [27–29]. In contrast to linear methods, nonlinear methods can bypass the spatial low-pass filter effects of the Green function and reconstruct high-contrast objects much more accurately. To make use of the high-frequency information in the superoscillatory field, we employ the CSI method to solve the inverse problem in this paper. Similar attempt is tried by combined OAM-carrying wave with joint sparse reconstruction, while OAM-carrying wave provides limited improvement in the method [30]. Moreover, the sparseness requirement limited the applied objects. The method in this paper does not rely on sparse *a-priori* information and works on most objects.

The outline of this paper is as follows. The theory of making use of high frequency information to improve the imaging profile is proposed in Section 2. Then, the designing of the superoscillatory field is studied in Section 3. A method of moments (MOM) simulation is implemented to verify the proposed method in Section 4, and some physical insights on the method are also given. In Section 5, some conclusive remarks are discussed.

2. The use of high-frequency information

The information of evanescent wave in measurement data and its involvement in the inversion algorithms are considered as the main reasons for superresolution [24]. However, superoscillation provides another opportunity to keep high-frequency information in the nonlinear inversion algorithms.

A typical 2D inverse scattering problem is shown in Fig. 1. T/R in Fig. 1 is transmitters and receivers. Region D is the region of interest (ROI) where the probed objects are located, and circle C is where the receivers and transmitters are located. Transmitters emit the single-frequency wave simultaneously, and receivers measure the steady-state scattering field. Because the objects are surrounded by these transmitters and receivers on circle C, the Field of View in this configuration is the region in circle C. The cylindrical objects S with arbitrary cross sections are inhomogeneous in the (x, y) plane but homogeneous along the z axis. The incident wave is a TM wave, which simplifies the problem into a scalar equation. The sources in Fig. 1 are line sources.

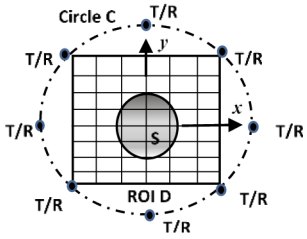

Fig. 1. The geometrical configuration adopted to study the inverse-scattering problem.

According to the volume equivalence principle, the scattering field is the radiation of the equivalent source. Without loss of generality, the objects are assumed to be nonmagnetic to

Optics EXPRESS

simplify the problem and are modeled as a contrast function

$$\chi(\boldsymbol{r}) = [\varepsilon_r(\boldsymbol{r}) - 1] - j\frac{\sigma(\boldsymbol{r})}{\omega\varepsilon_0}. \tag{1}$$

Here, ε_r $(\boldsymbol{r})$ is the relative permittivity of the objects; σ $(\boldsymbol{r})$ is the conductivity of scatters; ω is the angular frequency of the time-harmonic wave; and ε_0 is the permittivity in free space. The contrast functions χ $(\boldsymbol{r}) = 0$ on the condition that $\boldsymbol{r}$ is outside of the objects S. The contrast function and the incident field E^{inc} $(\boldsymbol{r})$ have the following relationship that

$$E(\boldsymbol{r}) = E^{inc}(\boldsymbol{r}) + k_0^2 \int_D G_0(\boldsymbol{r}, \boldsymbol{r}')\chi(\boldsymbol{r}')E(\boldsymbol{r}')d\boldsymbol{r}'. \tag{2}$$

Here, E $(\boldsymbol{r})$ is the total field, where $\boldsymbol{r}$ is the observation point belonging to region D; G_0 $(\boldsymbol{r}, \boldsymbol{r}')$ is the Green function in free space, where $\boldsymbol{r}'$ is the source point belonging to region D; and k_0 is the wavenumber in free space. Eq. (2), which shows the process of scattering, is the equation of state. The equation of measurement on circle C is given as

$$E_C^s(\boldsymbol{r}) = k_0^2 \int_D G_0(\boldsymbol{r}, \boldsymbol{r}')\chi(\boldsymbol{r}')E(\boldsymbol{r}')d\boldsymbol{r}'. \tag{3}$$

The inverse-scattering imaging problem involves acquiring the contrast function by solving the measurement equation. Because the total field $E(\boldsymbol{r})$ is coupled with the contrast function $\chi(\boldsymbol{r})$ in the state equation, solving the measurement equation that consists of $E(\boldsymbol{r})$ and $\chi(\boldsymbol{r})$ is a nonlinear inverse problem, which can be solved by CSI method [28].

As the objects exist in region D only, the measurement in (3) is contributed by the integral only in region D, which makes it possible to extend the integral region to full space with the assumption that E $(\boldsymbol{r}) = 0$ $(\boldsymbol{r} \notin \mathrm{D})$. Assume that the objects are in a lossless and homogeneous medium and that the permittivity does not change with the frequency. Then, Eq. (3) can be rewritten as the convolution between the Green function and the contrast source. Taking the two-dimensional Fourier transform of (3) with respect to (x, y) leads to

$$\begin{aligned} \tilde{E}^s(k_x, k_y) &= \tilde{G}_0(k_x, k_y) \cdot \tilde{w}(k_x, k_y) \\ \tilde{w}(k_x, k_y) &= \tilde{E}(k_x, k_y) * \tilde{\chi}(k_x, k_y) \end{aligned}, \tag{4}$$

where,

$$\tilde{E}(k_x, k_y) = \int_D E(x, y) \cdot e^{-j\boldsymbol{k}\cdot\boldsymbol{r}} d\boldsymbol{r}. \tag{5}$$

$\tilde{E}^s$, $\tilde{G}_0$, $\tilde{w}$ and $\tilde{\chi}$ are the Fourier transforms of the scattering field, Green function, contrast source and contrast function, respectively. '$*$' denotes the convolution. Due to the low-pass filtering effects of the Green function $\tilde{G}_0$ in (4), only low frequency part $|(k_x, k_y)| \le k_0$ of $\tilde{w}$ contributes to the scattering field $\tilde{E}^s$ that can be measured. Supposing total field E possesses superoscillatory component in region D, the Short-Term Fourier Transform of E in ROI is beyond k_0. Then, the part of $\tilde{\chi}$ above k_0 is also transformed to the low frequency component of $\tilde{w}$ by the convolution with superoscillatory $\tilde{E}$. A simple example is given in discrete form. Supposing the spectrum of the contrast function is constant. And the bandwidth of total field $\boldsymbol{E}_1$ is two discrete grids, while the bandwidth of $\boldsymbol{E}_2$ is one discrete grid. According to (4), the spectrums of scattering fields are

$$\begin{aligned} \tilde{E}_{s1} &= (\tilde{E}_1 * \tilde{\chi}) \cdot \tilde{G}_0 \\ &= \left(\begin{bmatrix} 0 & 1 & 0 \\ 1 & 1 & 1 \\ 0 & 1 & 0 \end{bmatrix} * \begin{bmatrix} 1 & 1 & 1 \\ 1 & 1 & 1 \\ 1 & 1 & 1 \end{bmatrix} \right) \odot \begin{bmatrix} 0 & 0 & 0 \\ 0 & 1 & 0 \\ 0 & 0 & 0 \end{bmatrix} \\ &= \begin{bmatrix} 3 & 4 & 3 \\ 4 & 5 & 4 \\ 3 & 4 & 3 \end{bmatrix} \odot \begin{bmatrix} 0 & 0 & 0 \\ 0 & 1 & 0 \\ 0 & 0 & 0 \end{bmatrix} = \begin{bmatrix} 0 & 0 & 0 \\ 0 & 5 & 0 \\ 0 & 0 & 0 \end{bmatrix} \end{aligned} \quad \begin{aligned} \tilde{E}_{s2} &= (\tilde{E}_2 * \tilde{\chi}) \cdot \tilde{G}_0 \\ &= \left(\begin{bmatrix} 0 & 0 & 0 \\ 0 & 1 & 0 \\ 0 & 0 & 0 \end{bmatrix} * \begin{bmatrix} 1 & 1 & 1 \\ 1 & 1 & 1 \\ 1 & 1 & 1 \end{bmatrix} \right) \odot \begin{bmatrix} 0 & 0 & 0 \\ 0 & 1 & 0 \\ 0 & 0 & 0 \end{bmatrix}, \\ &= \begin{bmatrix} 1 & 1 & 1 \\ 1 & 1 & 1 \\ 1 & 1 & 1 \end{bmatrix} \odot \begin{bmatrix} 0 & 0 & 0 \\ 0 & 1 & 0 \\ 0 & 0 & 0 \end{bmatrix} = \begin{bmatrix} 0 & 0 & 0 \\ 0 & 1 & 0 \\ 0 & 0 & 0 \end{bmatrix} \end{aligned} \tag{6}$$

Optics EXPRESS

which shows that compared with $\tilde{E}_2$, $\tilde{E}_1$ shifts more high frequency component of $\tilde{\chi}$ into low-pass filter $\tilde{G}_0$. Thus, retaining more high frequency information of the objects $\tilde{\chi}$ involved in $\tilde{E}^s$ requires wider bandwidth of $\tilde{E}$. The higher the oscillation frequency is, the higher the resolution is, regardless of the specific spatial waveform.

Furthermore, the spatial spectrum of the total field is

$$\tilde{E} = \tilde{E}^{inc} + \tilde{G}_0 \cdot \tilde{w}. \tag{7}$$

Since the Green function performs as a low-pass filter with bandwidth k_0, the superoscillation part in the total field comes from the incident field, which makes it possible to achieve superresolution with a superoscillatory incident field. In conclusion, the superoscillation effects in the incident field can increase the high frequency information possessed by the equivalent sources and result in a profile with higher resolution.

3. Designing a superoscillatory field with single-frequency sources

As shown in Fig. 1, the incident wave is excited by line sources around the ROI and can be formulated as a weighted sum of the Hankel function as

$$E^{inc}(\boldsymbol{r}) = -\frac{\omega_0 \mu_0}{4} \sum_{n=0}^{N-1} c_n H_0^{(2)}[k_0(\boldsymbol{r} - \boldsymbol{r_n})]. \tag{8}$$

Here, the zeroth-order second-kind Hankel function $H_0^{(2)}[k_0(\boldsymbol{r} - \boldsymbol{r}_n)]$ is the *n-th* line source at position $\boldsymbol{r_n}$, and c_n is the complex excitation. In addition, N is the number of sources. As the field is time-harmonic with wavenumber k_0, time harmonic factor exp $(j\omega_0 t)$ can be ignored. We constrain the position of sources in the circle around the ROI with the radius R, and the construction depends only on the excitation c_n of the sources.

We proved that a line source is a bandlimited function firstly. A 2D Fourier transform of the radially symmetric line source can be simplified into a zeroth-order Hankel transform

$$\begin{aligned} \mathcal{F}_2\{H_0^{(2)}(k_0\boldsymbol{r})\} &= \lim_{R\to\infty} \int_0^R r H_0^{(2)}(k_0 r) J_0(k_r r) dr \\ &= \lim_{R\to\infty} \frac{R}{k_0^2 - k_r^2} [k_r J_1(k_r R) H_0^{(2)}(k_0 R) - k_0 H_1^{(2)}(k_0 R) J_0(k_r R)], \end{aligned} \tag{9}$$

where k_r is the radial variable of spatial spectrum in cylindrical coordinate and R is the size of the transform window. When $k_r = k_0$, the spectrum is

$$\mathcal{F}_2\{H_0^{(2)}(k_0\boldsymbol{r})\} = \lim_{R\to\infty} \frac{R^2[J_1^2(k_0 R) + J_0^2(k_0 R) + e^{j\pi/2}]}{2}. \tag{10}$$

When k_r approaches k_0, the spectrum in (9) shows high order growth regardless of R. Thus, the spectrum of a line source is a circle with radius k_0. Radial distribution of the spectrum is shown in Fig. 2.

Consequently, the frequency of the fields excited by line sources is k_0. However, the bandwidth is a global property of the waveform. With given band limit, superoscillation is a locally waveform and must exist alongside high energy sidebands [31–33]. On the other hand, truncating the high energy sidebands can increase the bandwidth. Therefore, the fast varying waveform in ROI can be simply represented by windowed Fourier Transform [34], of which the transform window is ROI. Such spectrum of the field beyond k_0 indicates the existence of superoscillatory field in ROI.

Optics EXPRESS

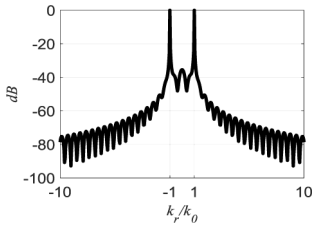

Fig. 2. The spectrum of a line source versus k_{r}, and the amplitude is normalized and logarithm with 20log(·).

The spectrum of the incident wave within the ROI [-*R*/2, *R*/2] can be written as

$$\begin{aligned} F_2\{E^{inc}(\boldsymbol{r})\} &= \int_{-R/2}^{R/2}\int_{-R/2}^{R/2} E^{inc}(\boldsymbol{r})\exp(-j\boldsymbol{k}\bullet\boldsymbol{r})d\boldsymbol{r} \\ &= -\tfrac{\omega_0\mu_0}{4}\sum_{n=0}^{N-1} c_n \int_{-R/2}^{R/2}\int_{-R/2}^{R/2} H_0^{(2)}[k_0(\boldsymbol{r}-\boldsymbol{r_n})]\exp(-j\boldsymbol{k}\bullet\boldsymbol{r})d\boldsymbol{r}. \end{aligned} \tag{11}$$

Equation (11) can be discretized in matrix form as

$$\boldsymbol{b} = \boldsymbol{A}\boldsymbol{c}. \tag{12}$$

where the vectors in the spectrum domain $\boldsymbol{k}$ and the spatial domain $\boldsymbol{r}$ are discretized into vectors k_{m} and r_{n}. Here, $\boldsymbol{A} = [F_2\{H_0^{(2)}[k_0(\boldsymbol{r}-\boldsymbol{r}_n)]\}]_{M\times N}$ is the spectrum of the line sources with limited observation that can be numerically calculated; $\boldsymbol{c} = [c(r_n)]_{N\times 1}$ is the complex excitation vectors of sources; $\boldsymbol{b} = [b(k_m)]_{M\times 1}$ is the discretized objective spectrum; N is the number of the sources and M is the number of the grids.

Because of the uncertainty relation between the spatial domain and the spectrum domain, there is a tradeoff between the tightly localized ROI and the tightly localized spectrum [34]. A R×R size ROI results in an spectrum with resolution $2\pi/R$. As superoscillation effects exist only in small regions, the spectrum does not have enough resolution to be interpolated. Thus, fitting a spectrum with superoscillation is an ill-posed problem. To overcome this problem, the wideband objective spectrum $\boldsymbol{b}$ is broken down into L discrete spectral points and $\boldsymbol{b} = \boldsymbol{b}_1 + \boldsymbol{b}_2 + \ldots + \boldsymbol{b}_{\mathrm{L}}$. Optimization is performed at each of spectral points and produces the excitation normalized to the corresponding spectral point. Although fitting a blurred spectrum $\boldsymbol{b}$ makes (12) an ill-posed problem, it is much easier to interpolate a spectrum $\boldsymbol{b}_l$ with single frequency point. The excitation for the wideband objective spectrum can be acquired from the summation of normalized excitations for discrete spectral points.

Moreover, high energy sidebands of superoscillation results in fast-varying zeros in the waveform vulnerable to noise [35]. For instance, superoscillatory part in OAM-carrying wave is the center zero and the center hole. The size of the hole in OAM-carrying wave increases with the modes. However, the amplitudes lower than noise can spoil the results in imaging. To avoid a large number of low amplitude parts appeared in the waveform, the amplitude of waveform at each point has to be optimized as well. As $\boldsymbol{b}$ is the spectrum of the incident field E^{inc} in the ROI, $||\boldsymbol{E}^{inc}||_2^2 = ||\boldsymbol{b}||_2^2$ is established according to Parseval's equation, which restricts the summation of amplitude squares for M points. Thus, a given upper bound of the amplitude can equivalently be a restriction on the size of the holes. In an extreme case, the waveform is composed of one maximum value and M-1 minimum values as

$$E^{inc}(r_m) = \begin{cases} \max(E^{inc}) & r_m = r_0 \\ \min(E^{inc}) & others \end{cases}, \tag{13}$$

Optics EXPRESS

of which the maximum value also is the upper bound of the amplitudes in the other cases with the same dynamic range and total energy $||\boldsymbol{b}||_2^2$. With given dynamic range d, the maximum value max (E^{inc}) in the extreme case is $||\boldsymbol{b}||_2/[1+(M-1)/d]$ that is also an upper bound of other amplitudes with the same dynamic range. Above all, the optimization is

$$\begin{aligned} &\min \ ||\boldsymbol{A}_l\boldsymbol{c}_l - \boldsymbol{b}_l||_2^2 \\ &s.t. \ ||\boldsymbol{E}^{inc}(r_m)||_2^2 \le ||\boldsymbol{b}||_2^2 d^2 / (M-1+d^2) \quad r_m \in ROI \end{aligned} . \tag{14}$$

where $\boldsymbol{A}_l$ is the spectrum of the line sources at frequency point $\boldsymbol{k}_l$. Since $\boldsymbol{b}=\boldsymbol{b}_1+\boldsymbol{b}_2+\ldots+\boldsymbol{b}_{\text{L}}$, $\boldsymbol{c}=\boldsymbol{c}_1+\boldsymbol{c}_2+\ldots+\boldsymbol{c}_{\text{L}}$ is the excitation for the wideband spectrum $\boldsymbol{b}$.

The performance of this construction method is examined as follows. Our test domain D consists of a square with sides of length λ_0 (specified in terms of wavelength), while the measurement curve C is a circle of radius $3\lambda_0$ whose center is at the center of D. The discrete form of the algorithm is obtained by dividing D into 30×30 subsquares. The wavenumber $|k_0|=2\pi f_0/c$ is the spatial bandwidth of the field. The 40 line sources are equally spaced in the measurement curve. The wideband objective spectrum is set as $[-3k_0, 3k_0]$. The dynamic range is set as $d=1000$. The construction results are depicted in Fig. 3.

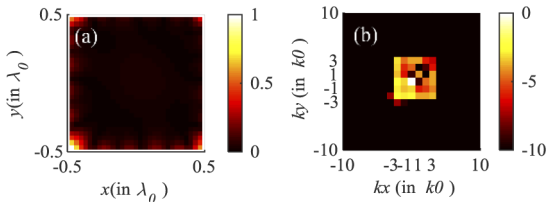

Fig. 3. (a) The designed superoscillatory waveform. The coordinate is normalized according to λ_0; (b) 2D-FFT of the designed superoscillatory waveform in the ROI. The coordinates in (b) is normalized according to k_0, and the range of spectrum is constrained to $(-10k_0, 10k_0)$. Amplitude in (b) is normalized and logarithm with 20log(·).

Fig. 3(a) is the designed waveform in ROI with range $[-\lambda_0, \lambda_0]$. Figure 3(b) is the spectrum of the field excited by optimized sources with $3k_0$ bandwidth. The axes in Fig. 3(b) is normalized to k_0. It is clear that the optimized waveform possesses a bandwidth covering $[-3k_0, 3k_0]$, which indicates the existence of superoscillation in the ROI and the effectiveness of proposed method.

As a natural superoscillatory waveform, the OAM-carrying field possesses fast-varying edges around the center zero of the vortex [10]. We compared the waveform of the OAM-carrying field with the 2D superoscillation designed. The distribution of sources is the same as the source distribution in the previous example. The phase difference between two adjacent sources to be $\delta\phi = 2\pi l/N$, where l is the topological charge. The OAM-carrying field can be formulated as the sum of line sources with different initial phases as

$$E^{inc}(\boldsymbol{r}, l) = \sum_{n=1}^{N} H_0^{(2)}(k_0|\boldsymbol{r}-\boldsymbol{r}_n|)\exp(jl\cdot n\cdot\delta\phi), \tag{15}$$

where $\boldsymbol{r}_n$ is the position of the *n-th* line source. The OAM-carrying fields with $l=0$, 3, 5 and their 2D Fourier transformations in the ROI are shown in Fig. 4.

In Fig. 4(d) and Fig. 4(e), the spectrums of OAM-carrying fields with $l=0$ and $l=3$ are limited around $[-k_0, k_0]$. In Fig. 4(f), OAM-carrying fields with $l=5$ possess high spatial frequency components beyond k_0, which indicates that the higher the modes, the higher the spectrums. However, the amplitude of OAM-carrying field is inhomogeneous in ROI and varies with modes.

Optics EXPRESS

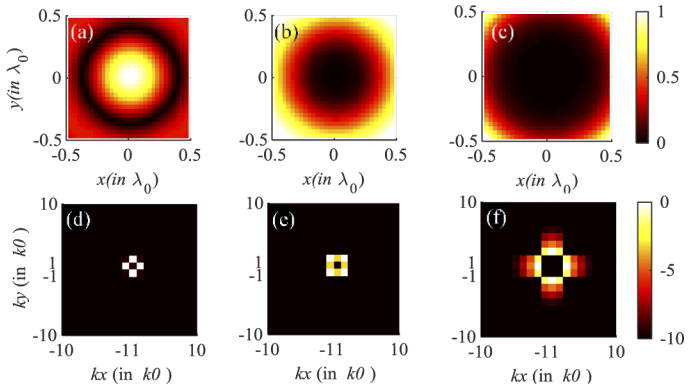

Fig. 4. (a) OAM-carrying field with modes $l = 0$; (b) OAM-carrying field with modes $l = 3$; (c) OAM-carrying field with modes $l = 5$; (d) The 2D Fourier transformation of the OAM-carrying field (a) in the ROI. (e) The 2D Fourier transformation of the OAM-carrying field (b) in the ROI. (f) The 2D Fourier transformation of the OAM-carrying field (c) in the ROI. Amplitudes in (d), (e) and (f) are normalized and logarithm with 20log(·).

OAM-carrying field excited by M sources on the circle with radius R is

$$E_l^{inc}(\boldsymbol{r}) = \sum_{m=0}^{M-1} c_m H_0^{(2)}[k_0|R-\boldsymbol{r}|] = \sum_{m=0}^{M-1} c_m \sum_{n=-\infty}^{+\infty} H_n^{(2)}(k_0R)J_n(k_0r)e^{jn(\varphi_m-\varphi)}, \tag{16}$$

where c_m is the excitation coefficient of the *m-th* source. For transmitters with dense distribution, the summation in (16) can be transformed into integral on the curve of sources

$$E_l^{inc}(\boldsymbol{r}) = \int_0^{2\pi} e^{jl\varphi'} \sum_{n=-\infty}^{+\infty} H_n^{(2)}(k_0R)J_n(k_0r)e^{jn(\varphi'-\varphi)}d\varphi' = H_l^{(2)}(k_0R)J_l(k_0r)e^{jl\varphi}. \tag{17}$$

According to Graf's Addition Theorem, the summation of (17) over modes is

$$\begin{gathered}\sum_{l=-\infty}^{+\infty} E_l^{inc}(\boldsymbol{r}) = \sum_{l=-\infty}^{+\infty} H_l^{(2)}(k_0R)J_l(k_0r)e^{jl\varphi} = H_0^{(2)}(k_0r') \\ r' = \sqrt{r^2+R^2-2Rr\cos\varphi}\end{gathered}. \tag{18}$$

Thus, the summation of OAM-carrying fields is not a function with wide bandwidth. From the perspective of superoscillation, the OAM-carrying fields with lower modes perform the role of high energy sidebands which exist alongside superoscillation and pull down the spatial frequency of the field in ROI. The 2D Fourier transformations of the OAM-carrying fields with summation over $l = 0, \pm1, \ldots, \pm10$ and summation over $l = \pm5, \ldots, \pm10$ are shown in Fig. 5.

The spatial spectrum of OAM-carrying field with modes $l = 0, \pm1, \ldots, \pm10$ is k_0 [see Fig. 5(b)], while the spatial spectrum of OAM-carrying field without lower modes is much higher [see Fig. 5(d)]. On the other hand, OAM-carrying field with modes $l = \pm5, \ldots, \pm10$ lacks the low frequency spectrums. As most objects possess low frequency component, lacking of low frequency components in the illumination results in the deterioration of profiles. Furthermore, OAM-carrying wave is only decided by the topological charge, of which the spatial spectrum cannot be adjusted according to ROI.

Optics EXPRESS

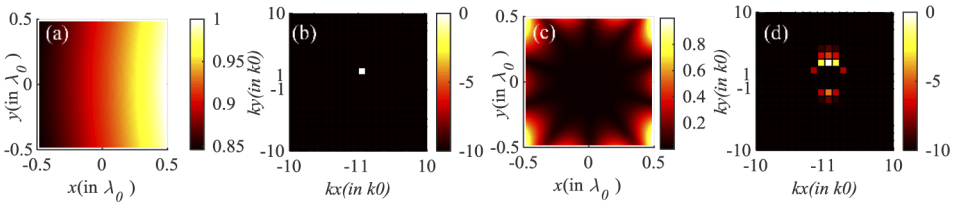

Fig. 5. (a) The sum of the OAM-carrying field with modes $l = 0, \pm 1, \ldots, \pm 10$; (b) The 2D Fourier transformation of the OAM-carrying field in (a); (c) The sum of the OAM-carrying field with modes $l = \pm 5, \ldots, \pm 10$; (d) The 2D Fourier transformation of the OAM-carrying field in (c). Amplitudes in (b) and (d) are normalized and logarithm with $20\log(\cdot)$.

4. Results and discussions

In this section, we provide the simulated results under the excitations designed in part 3. The condition of imaging remains the same as the condition of designing. The forward problem is solved with the CG-FFT method to acquire the measurement data [36]. As the equation in the CG-FFT method is different from the equation in the inverse problem, the inverse crime is avoided. The 40 line sources are equally spaced in the measurement circle, and the frequency is f_0 without specified value, for the following results are normalized according to the frequency. The scattering field is measured by 80 receivers on the measurement circle. The test domain D is a square with side length λ_0, while the measurement circle C is a circle of radius $3\lambda_0$ and has the same center as region D. The discrete form of CSI is obtained by dividing D into 30×30 subsquares. We test the performance of our method on complex objects in this example and compare it with those of incident fields excited by line sources in turns and the OAM-carrying incident field. To gather up enough times of illuminations, the designed excitation $\boldsymbol{c_l}$ in (14) at each spectrum point $\boldsymbol{b_l}$ is applied rather than the sum of excitations $\boldsymbol{c}$, which provides L incident fields. The sum of L incident fields is the wide band spectrum in Fig. 3(b).

For comparison, classical CSI method is applied with the same imaging configuration in Fig. 1. In classical CSI method, the incident field is excited by one of 40 line sources, and the scattering field is measured by all 80 receivers simultaneously [29], which provide one group of measurement data. Because 40 line sources are applied in our construction of superoscillatory field, to make comparison fair, 40 incident fields excited by different line sources are applied in classical CSI, which ensures the same aperture with designed fields and is a Multiple Input and Multiple Output system. Therefore, 40 groups of measurement data are made with the incident fields excited by 40 line sources in turns. Then, the state equation [Eq. (2)] and the measurement equation [Eq. (3)] are solved by iteration. Because each of incident fields is excited by single source, the spatial spectrum of each incident field in ROI is k_0. Moreover, the sum of 40 incident fields in classical CSI is equal to an OAM-carrying field with $l = 0$ [see Fig. 4(a)] and possesses no superoscillation effects.

Generated by the same 40 line sources, OAM-carrying fields with $l = 0, \pm 1 \ldots \pm 10$ and the ones with $l = \pm 5 \ldots \pm 10$ are also used for comparison.

4.1. Two dielectric squares

The imaged objects are two dielectric squares cylinders with side lengths $7\lambda_0/30$, and the sides of both objects are 45 degrees from the x-axis. The contrast of both objects is $\chi = 4$, and the original profile of the object is shown in Fig. 6(a).

Four profiles are computed with 256 iterations by CSI method, and the results are shown in Fig. 6. The profile in Fig. 6(e) is the result of the incident wave designed in this paper. Figure 6(b) shows the profile without the superoscillation. Figure 6(c) is the results of OAM-carrying field

Optics EXPRESS

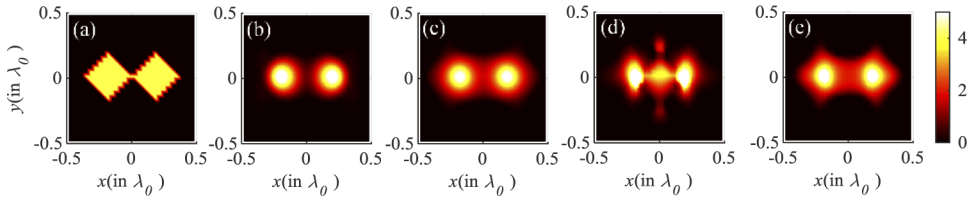

Fig. 6. Imaging of the two objects. (a) The original contrast profile; (b) The contrast profile reconstructed with incident wave excited by line sources in turns; (c) The contrast profile reconstructed with the OAM-carrying fields $l = 0, \pm 1, \ldots, \pm 10$; (d) The contrast profile reconstructed with the OAM-carrying fields $l = \pm 5, \ldots, \pm 10$; (e) The contrast profile reconstructed with designed superoscillatory field.

with $l = 0, \pm 1 \ldots \pm 10$. Figure 6(d) is the results of OAM-carrying field with $l = \pm 5 \ldots \pm 10$. The fine details of the squares are blurry in Fig. 6(b) and Fig. 6(c), which indicates the missing of superoscillation effects in OAM-carrying field with $l = 0, \pm 1 \ldots \pm 10$. On the other hand, the vertical edges on the left and right sides of the objects have remained in Fig. 6(e), which shows that the profile reconstructed with superoscillatory illumination is closer to the shape of the original profile. In contrast, the result of OAM-carrying field with $l = \pm 5 \ldots \pm 10$ in Fig. 6(d) is worse than the one with $l = 0, \pm 1 \ldots \pm 10$. Due to the lacking of low frequency components, the result of Fig. 6(d) is tracked in local optimums in iterations.

In order to show the mechanism of high frequency information applied in this example, Fig. 7 shows the two-dimensional Fourier transform of the sum of total fields over all times illuminations and the sum of contrast sources over all times illuminations in each method, which reports the local spectrums in range of $[-\lambda_0/2, \lambda_0/2]$. The results are normalized and depicted with logarithm amplitude ranging from -10 dB to 0 dB to show the bandwidth of the waveforms. The spectrums of contrast sources are the convolutions between the spectrums of total fields and the spectrums of contrasts in (4).

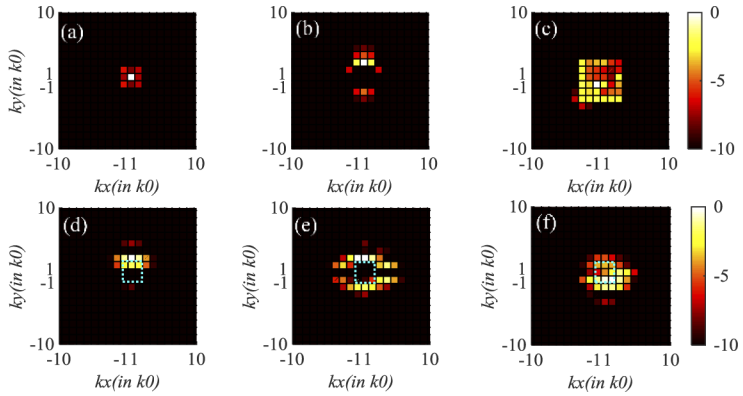

Fig. 7. 2D-FFT of the sum of total fields and the sum of contrast sources: (a) Spectrum of the sum of total fields in classical-CSI; (b) Spectrum of the sum of total fields in OAM-CSI with $l = \pm 5, \ldots, \pm 10$; (c) Spectrum of the sum of total fields in Superoscillation-CSI; (d) Spectrum of the sum of contrast sources in normal-CSI; (e) Spectrum of the sum of contrast sources in OAM-CSI with $l = \pm 5, \ldots, \pm 10$; (f) Spectrum of the sum of contrast sources in Superoscillation-CSI. Amplitudes in (d), (e) and (f) are normalized and logarithm with $20\log(\cdot)$. The thin cyan dot lines in (d), (e) and (f) are the indications of the low-pass band of Green function.

Optics EXPRESS

Due to the superoscillation effects in the incident waves, the spatial spectrum of the total fields in Superoscillation-CSI method [see Fig. 7(c)] and OAM-CSI method with $l = \pm 5 \ldots \pm 10$ [see Fig. 7(b)] are much higher than that of classical-CSI method [see Fig. 7(a)]. Such high spatial frequency makes it easier to convolute high frequency components of objects into the contrast sources, and retains this high frequency information under the low-pass filtering effects of the Green function. Compared with designed superoscillatory wave, the bandwidth of OAM-carrying wave lacks the low frequency components. Thus, the total field spectrum in OAM-CSI method has a lack of low frequency components in $[-k_0, k_0]$ in the convolution $\tilde{E} * \tilde{\chi}$ [see Fig. 7(e)], which leads to the lack of most components after low-pass filtering of Green function and makes the result in Fig. 6(d) tracked in local optimums. In comparison, the spectrums of contrast sources in Superoscillation-CSI method are more focused on the low frequency part in $[-k_0, k_0]$ [see Fig. 7(f)]. Therefore, designed superoscillatory field works better than OAM-carrying field.

The spectrums of the original contrast and the reconstructed contrasts are depicted in Fig. 8, which also illustrate the quality of profiles. Due to the lack of low frequency component, the result of OAM-CSI with $l = \pm 5 \ldots \pm 10$ possesses false spectrum components [see Fig. 8(d)]. The spectrum of OAM-CSI with $l = 0, \pm 1 \ldots \pm 10$ is similar to the spectrum of classical CSI, which is consistent with our results in (18). In comparison, the spectrum of contrast reconstructed with designed superoscillatory incident wave is wider and closer to the original spectrum in Fig. 8(a).

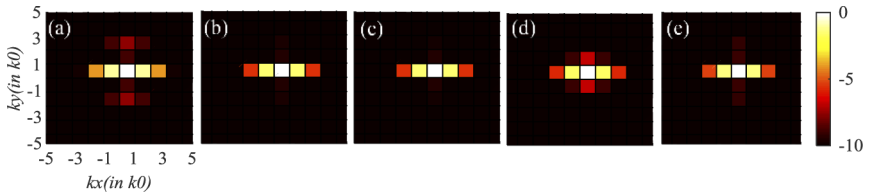

Fig. 8. 2D-FFT of the two objects. (a) Result of the original contrast; (b) Result of the contrast reconstructed by Classical-CSI; (c) Result of the contrast reconstructed by OAM-CSI with $l = 0, \pm 1, \ldots, \pm 10$; (d) Result of the contrast reconstructed by OAM-CSI with $l = \pm 5, \ldots, \pm 10$; (e) Result of the contrast reconstructed by Superoscillation-CSI. Amplitudes are normalized and logarithm with $20\log(\cdot)$.

4.2. Four dielectric squares

We test the performance of our method on complex objects in this example and the imaged objects are four dielectric squares cylinders with side lengths $7\lambda_0/30$ and $2\lambda_0/15$ spacing. The contrast of objects remain $\chi = 4$, and the original profile of the object is shown in Fig. 9(a). OAM-carrying fields with $l = \pm 5 \ldots \pm 10$ are not applied here for the defective results.

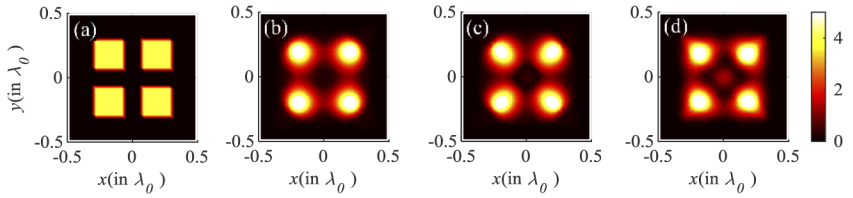

Fig. 9. Imaging of the four objects. (a) The original contrast profile of the objects; (b) The contrast profile reconstructed with incident wave excited by line sources in turns; (c) The contrast profile reconstructed with the OAM-carrying fields $l = 0, \pm 1, \ldots, \pm 10$; (d) The contrast profile reconstructed with designed superoscillatory field.

Optics EXPRESS

Iteration time remains the same as the previous example, and the results are shown in Fig. 9. The profile in Fig. 9(d) is the result of the incident wave designed in this paper and shows sharper edges compared with the other two results. The conception of making use of high frequency information is proved effective for the precise shape reconstruction. The intense dot in the center of Fig. 9(d) is the result of ringing effects. There are four narrow main lobes in Fig. 9(d), which results in the superposition of side lobes in the center. Because the bandwidth in Superoscillation-CSI is wider, the main lobe width in Fig. 9(d) is sharper, and ringing effects is stronger.

Though the nonlinear relationship between χ and E^s makes it unavailable to generally evaluate the effective of proposed method, with given objects, E^s is linear to E^{inc}, and the operators G_0E of different incident fields can be compared. Singular Value Decompositions (SVD) of the operators G_0E are presented in Fig. 10.

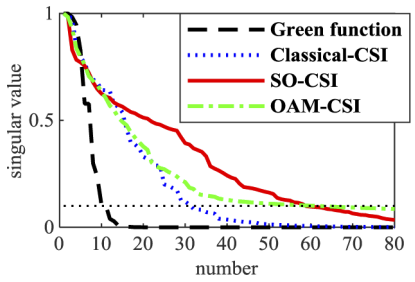

Fig. 10. The Singular Value Decomposition of operators G_0 and G_0E. X-axis is the number of singular values and y-axis is the normalized singular value. The black dash line is the SVD of G_0; The blue dot line is the SVD of G_0E in classical-CSI; The red line is the SVD of G_0E in Superoscillation-CSI; The green dash-dot line is the SVD of G_0E in OAM-CSI. The thin black dot line is the reference line of 0.1.

As the spectrum of the operator, distribution of singular values is an indication of the equation regularity. In regularization, small singular values are suppressed and corresponding high frequency information is lost for stability of solutions. Therefore, the more the large singular values, the more the high frequency information kept.

In Fig. 10, Green function possesses the least number of large singular values, which results in the Rayleigh limit. Number of large singular values in OAM-CSI is close to the one of Classical-CSI, while high frequency components in OAM-CSI are more than the ones of Classical-CSI. Consequently, the result of OAM-CSI has no distinct differences with the result of Classical-CSI. Compared with OAM-CSI, Superoscillation-CSI lacks highest frequency components but has sufficient middle frequency components to guarantee better results.

4.3. E-shape object

The imaged object is E-shape cylinder with size ($\lambda_0/3$, $3\lambda_0/5$). The contrast of objects remain $\chi = 4$, and the original profile of the object is shown in Fig. 11(a). Iteration time remains the same as the previous example, and the results are shown in Fig. 11. The profile in Fig. 11(d) also possesses sharper edges compared with the other two results.

To verify accuracy and convergency speed of the methods, the errors of contrasts in each iteration are shown in Fig. 12. The error is calculated as

$$Err = \frac{||\chi - \chi_0||}{||\chi_0||}, \tag{19}$$

where χ is the solved contrast function in ROI, and χ_0 is the true contrast function in ROI.

Optics EXPRESS

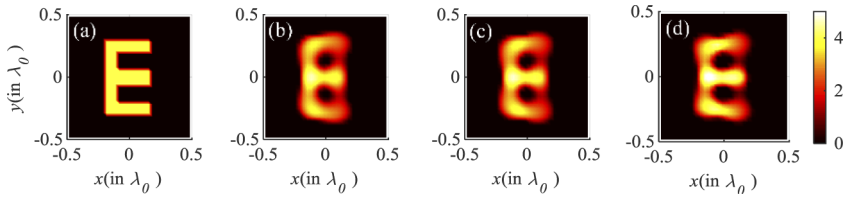

Fig. 11. Imaging of the E shape objects. (a) The original contrast profile of the objects; (b) The contrast profile reconstructed with incident wave excited by line sources in turns; (c) The contrast profile reconstructed with the OAM-carrying fields $l = 0, \pm 1, \ldots, \pm 10$; (d) The contrast profile reconstructed with designed superoscillatory field.

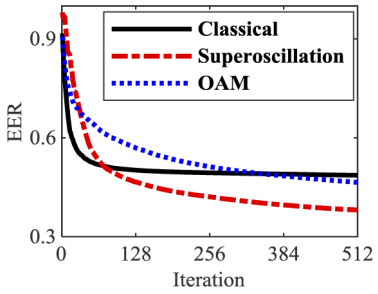

Fig. 12. The errors of contrast profiles in iterations.

The convergency speeds of three methods are the same due to no *a-priori* information included in the algorithm. As a physical super-resolution method, design of incident field does not constrain the solution space and has no acceleration on the convergency speed. However, the error of proposed method is smaller than other errors, which shows the improvement of reconstruction accuracy and indicates that a proper designed incident field can convolute more information into the bandlimited propagating waves.

5. Conclusion

In this paper, we have proposed a new method to apply superoscillation in microwave imaging. The mechanism of superresolution imaging with superoscillatory incident fields is studied at first. With the wide bandwidth of local incident fields, scattering field can keep high frequency information of the objects from the spatial filtering effects of the Green function by the convolution between the spectrum of objects and the local spectrum of total fields.

Then the superoscillatory field with a single frequency is synthesized by optimizing the spatial-spectrum domain, and the high-frequency information in the field is used by a nonlinear inverse-scattering method without the need to consider spatial waveforms. The numerical results show the effectiveness of the method and the improvement of the resolution. Comparisons with OAM-carrying waves that have a superoscillatory focus on the center zero show that the proposed method can achieve superresolution uniformly in the ROI.

Superoscillatory field is applied to increase the high frequency information convoluted within the bandwidth of scattering field, and the bandwidth of scattering field is still not be fully used so far. However, in the numerical examples, the imaging results indicate that the imaging quality is not only related to the local bandwidth of the total field, but also to the local spatial spectrum coverage of the total field. This conclusion shows the possibility of an ideal local spatial spectrum of total field that can fully fill the scattering field bandwidth with information of objects by convolution. Shannon's theorem allows superoscillatory information compression to a

Optics EXPRESS

bandlimited channel with demanding on the power, which gives a direct relationship between the imaging resolution and the power [34,37]. With the limitation of the power, choosing total field turns to the digital coding of local spatial spectrum of total field [38]. The optimization of total field remains to be further discussed. As a result, we will report further progress in the near future.

Funding

National Natural Science Foundation of China (61971392).

Acknowledgments

The authors would like to thank Chenyou Yin and Qimeng Fan for fruitful discussions. Our deepest gratitude goes to the anonymous reviewers for their careful work and thoughtful suggestions that have helped improve this paper substantially.

Disclosures

ABC: 123 Corporation (I,E,P), DEF: 456 Corporation (R,S). GHI: 789 Corporation (C).
The authors declare no conflicts of interest.

References

1. H. P. Baltes, "Inverse Scattering Problems in Optics," Opt. Acta. **20**, 1032–1033 (1980).
2. L. Rayleigh, "On the theory of optical images, with special reference to the microscope," Philos. Mag. **42**(255), 167–195 (1896).
3. E. Betzig, J. K. Trautman, T. D. Harris, J. S. Weiner, and R. L. Kostelak, "Breaking the diffraction barrier: optical microscopy on a nanometric scale," Science **251**(5000), 1468–1470 (1991).
4. J. B. Pendry, "Negative refraction makes a perfect lens," Phys. Rev. Lett. **85**(18), 3966–3969 (2000).
5. A. Hartschuh, E. J. Sanchez, X. S. Xie, and L. Novotny, "High-resolution near-field Raman microscopy of single-walled carbon nanotubes," Phys. Rev. Lett. **90**(9), 095503 (2003).
6. W. X. Jiang, C. W. Qiu, T. C. Han, Q. Cheng, H. F. Ma, S. Zhang, and T. J. Cui, "Broadband all-dielectric magnifying lens for far-field high-resolution imaging," Adv. Mater. **25**(48), 6963–6968 (2013).
7. J. Hunt, T. Driscoll, A. Mrozack, G. Lipworth, M. Reynolds, D. Brady, and D. R. Smith, "Metamaterial apertures for computational imaging," Science **339**(6117), 310–313 (2013).
8. L. Wang, L. Li, Y. Li, H. C. Zhang, and T. J. Cui, "Single-shot and single-sensor high/super-resolution microwave imaging based on metasurface," Sci. Rep. **6**(1), 26959 (2016).
9. F. M. Huang and N. I. Zheludev, "Super-resolution without evanescent waves," Nano Lett. **9**(3), 1249–1254 (2009).
10. E. T. Rogers, J. Lindberg, T. Roy, S. Salvatore, J. E. Chad, M. R. Dennis, and N. I. Zheludev, "A super-oscillatory lens optical microscope for subwavelength imaging," Nat. Mater. **11**(5), 432–435 (2012).
11. E. T. F. Rogers and N. I. Zheludev, "Optical super-oscillations: Subwavelength light focusing and super-resolution imaging," J. Opt. **15**(9), 094008 (2013).
12. K. S. Rogers, K. N. Bourdakos, and G. H. Yuan, "Optimising superoscillatory spots for far-field super-resolution imaging," Opt. Express **26**(7), 8095–8112 (2018).
13. Y. Kozawa, M. Matsunaga, and S. Sato, "Superresolution imaging via superoscillation focusing of a radially polarized beam," J. Opt. **5**(2), 86–92 (2018).
14. L. Li, F. Li, and T. J. Cui, "Computational superoscillation imaging beyond the Rayleigh limit from far-Field measurements," Opt. Express **22**(5), 5431–5441 (2014).
15. A. M. H. Wong and G. V. Eleftheriades, "Superoscillatory Radar Imaging: Improving Radar Range Resolution Beyond Fundamental Bandwidth Limitations," IEEE Microw. Wireless Compon. Lett. **22**(3), 147–149 (2012).
16. A. M. H. Wong, "Sub-Diffraction Imaging using Superoscillatory Electromagnetic Waves," Ph.D. dissertation, Dept. Elect. Compu. Eng., Toronto Univ., Toronto, Canada, 2014.
17. L. Li and F. Li, "Beating the Rayleigh limit: orbital-angular-momentum-based super-resolution diffraction tomography," Phys. Rev. E **88**(3), 033205 (2013).
18. A. M. H. Wong and G. V. Eleftheriades, "Adaptation of Schelkunoff's superdirective antenna theory for the realization of superoscillatory antenna arrays," IEEE Antennas Wireless Propag. Lett. **9**, 315–318 (2010).
19. A. M. H. Wong and G. V. Eleftheriades, "Temporal pulse compression beyond the Fourier transform limit," IEEE Trans. Microwave Theory Tech. **59**(9), 2173–2179 (2011).
20. D. G. Lee and P. J. S. G. Ferreira, "Direct Construction of Superoscillations," IEEE Trans. Signal. Proces. **62**(12), 3125–3134 (2014).

Optics EXPRESS

21. Q. Xie, Y. Jiang, J. Liang, E. Qu, and L. Ren, "Hybrid phase-amplitude superoscillation element for nonscanning optical superresolution imaging," J. Opt. Soc. Am. A **36**(2), 196–201 (2019).
22. X. H. Dong, A. M. H. Wong, M. Kim, and G. V. Eleftheriades, "Superresolution far-field imaging of complex objects using reduced superoscillating ripples," J. Opt. **4**(9), 1126–1133 (2017).
23. R. K. Amineh and G. V. Eleftheriades, "2D and 3D sub-diffraction source imaging with a superoscillatory filter," Opt. Express **21**(7), 8142–8156 (2013).
24. T. J. Cui, C. C. Weng, X. X. Yin, and W. Hong, "Study of resolution and superresolution in electromagnetic imaging for half-space problems," IEEE Trans. Antennas Propag. **52**(6), 1398–1411 (2004).
25. R. F. Harrington, *Time-Harmonic Electromagnetic Fields*. McGraw-Hill, New York, 1961.
26. M. Slaney, A. C. Kak, and L. E. Larsen, "Limitations of Imaging with First-Order Diffraction Tomography," IEEE Trans. Microwave Theory Tech. **32**(8), 860–874 (1984).
27. R. E. Kleinman and P. M. V. D. Berg, "Iterative methods for solving integral equations," Radio Sci. **26**(1), 175–181 (1991).
28. A. Abubakar and P. M. V. D. Berg, "The contrast source inversion method for location and shape reconstructions," Inverse Probl. **18**(2), 495–510 (2002).
29. S. Sun, B. J. Kooiji, T. Jin, and A. G. Yarovoy, "Cross-correlated Contrast Source Inversion," IEEE Trans. Antennas Propag. **65**(5), 2592–2603 (2017).
30. Q. Fan, C. Yin, and H. Liu, "Accurate Recovery of Sparse Objects With Perfect Mask Based on Joint Sparse Reconstruction," IEEE Access **7**, 73504–73515 (2019).
31. Y. Aharonov, F. Colombo, I. Sabadini, D. Struppa, and J. Tollaksen, "The mathematics of superoscillations," *Mem. Am. Math. Soc.* 247(1174), (2017).
32. M. Berry and P. Shukla, "Pointer supershifts and superoscillations in weak measurements," J. Phys. A: Math. Theor. **45**(1), 015301 (2012).
33. J. Tollaksen, "Novel relationships between superoscillations, weak values, and modular variables," J. Phys.: Conf. Ser. **70**(1), 012016 (2007).
34. A. Kempf, "Black holes, bandwidths and Beethoven," J. Math. Phys. **41**(4), 2360–2374 (2000).
35. M. V. Berry, "Suppression of superoscillations by noise," J. Phys. A: Math. Theor. **50**(2), 025003 (2017).
36. P. Zwamborn and P. M. V. D. Berg, "The Three-Dimensional Weak Form of the Conjugate Gradient FFT Method for Solving Scattering Problems," IEEE Trans. Microwave Theory Tech. **40**(9), 1757–1766 (1992).
37. P. J. S. G. Ferreira and A. Kempf, "Superoscillations: Faster than the Nyquist rate," IEEE Trans. Signal Process. **54**(10), 3732–3740 (2006).
38. M. E. Testorf, "Superresolution imaging and superoscillation design," *Imag. and Appl. Opt.*, MW1D.3 (2019).